Magnetic Equivalent Circuit and Lagrange Interpolation Function Modeling of Induction Machines Under Broken Bar Faults

Ahmed Hemeida[1,2], Md Masum Billah[1], Karolina Kudelina[3], Bilal Asad[3], Muhammad U Naseer[3], Baocheng Guo[4], Floran Martin[1], Paavo Rasilo[5], and Anouar Belahcen[1], Senior Memeber, IEEE
[1]Department of Electrical Engineering and Automation, Aalto University, FI-00076, Espoo, Finland
[2]Department of Electrical Engineering, Cairo University, 12613, Al-Jizah, Egypt
[3]Department of Electrical Power Engineering and Mechatronics, Tallinn University of Technology, 19086 Tallinn, Estonia
[4]School of Electrical and Automation Engineering, Nanjing Normal University, 210096 China
[5]Electrical Engineering Unit, Tampere University, FI-33014 Tampere, Finland

This paper introduces a mesh-based magnetic equivalent circuit (MEC) modeling technique for induction machines (IMs) in healthy and broken rotor bars conditions. The MEC model is presented as a highly accurate and computationally efficient alternative to finite element (FE) models. By incorporating modifications to the air gap coupling method, including a new Lagrange interpolation function, and utilizing a harmonic MEC model, the accuracy of the solution is improved while reducing electrical and mechanical transients. Compared to experiments and 2D FE models, this model achieves precise results for electromagnetic torque, rotational speed, and forces across various conditions. The Lagrange interpolation function forms the basis for the air gap coupling between stator and rotor flux densities. The results demonstrate the MEC model's exceptional accuracy in predicting speed oscillations, calculating forces, and analyzing current harmonics in faulty IMs. Furthermore, the MEC model performs over 30 times faster than the 2D FE models.

***Index Terms*—Broken rotor bar faults, induction machines, magnetic equivalent circuit (MEC), non-linear, reluctance network (RN).**

I. Introduction

INDUCTION MACHINES (IMs) are extensively employed in various applications owing to their reliability. As a result, multiple modeling techniques have been developed over time. While finite element (FE) models offer high accuracy [1], they may not be the most efficient tool for quick results during initial machine design or real-time simulation integration. Consequently, analytical tools have been devised [1], [2]. A comprehensive overview of these models, covering various types of faults in IMs, can be found in [1].

The magnetic equivalent circuit (MEC) model [3], [4] offers a valuable alternative in electric machine modeling. It strikes a balance between accuracy and computational efficiency by providing higher accuracy than analytical models while requiring fewer computational resources compared to FE models. However, the study presented in [4] indicates that while the computational times are low, the accuracy of torque ripple prediction falls short compared to 2D FE models. Additionally, the forces generated in different fault scenarios were not included in any of the models discussed. These forces can be crucial for conducting further vibration analysis of electric machines, as highlighted in [5].

The Lagrange interpolation function described in [6] for the MEC model is used for coupling the stator and rotor nodes. This technique is applied to the nodal-based MEC for permanent magnet machines. Raising the interpolation order in the Lagrange function has been observed to result in instability in the solution and necessitates a greater number of iterations to attain the desired tolerance. This article presents modifications made to the air gap coupling method described in [6] for the mesh-based MEC. Instead of considering only the central angle in the Lagrange function, the approach now involves dividing each block into multiple angles and taking the average of the Lagrange function. This modification ensures a highly accurate solution. This approach is applied in this study to analyze various broken bar faults in IMs. The paper provides a description of the air gap coupling methodology and the stator and rotor electric circuit equations. Furthermore, a harmonic MEC model is developed to initialize the time-stepping MEC and minimize mechanical and electrical transients. Non-linear iterations are handled using the Newton-Raphson technique.

Corresponding author: A. Hemeida (email: a.hemeida@ieee.org).

II. MEC Model Introduction

The MEC models for a stator and a rotor tooth are depicted in Figs. 1 (a) and (b) respectively. The magneto-motive forces (MMFs) $F_{\mathrm{s}}(d,1\text{-}2)$ and $F_{\mathrm{s}}(d{+}1,1\text{-}2)$ in Fig. 1 (a), correspond to stator slots d and d+1. They increase linearly from the bottom of the slot to their maximum values at the stator yoke. Similarly, the induced loop currents in the rotor bars, illustrated in Fig. 1 (b), are associated with the MMFs $F_{\mathrm{r}}(c,1\text{-}3)$ and $F_{\mathrm{r}}(c{+}1,1\text{-}3)$ of rotor bars c and c+1. The MEC model adopts varying circumferential elements in the radial direction.

The model incorporates the non-linear behavior of the iron material using the Newton-Raphson technique. The non-linear elements are represented by the red-colored reluctances [7]. In addition, the rotor skewing effect is modeled using the multi-slice 2D modeling approach [7]. To account for the impact of broken rotor bar conditions on mechanical transients, the model takes the mechanical torque as input and adjusts the rotational speed based on the electromagnetic output torque of the model and the system's mechanical inertia.

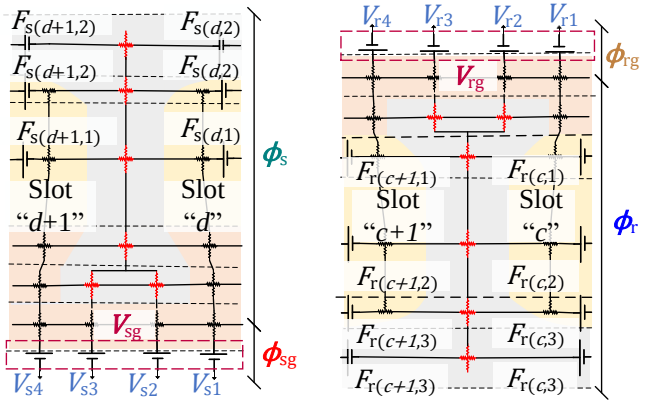

(a) Stator MEC (b) Rotor MEC

Fig. 1. MEC models for the stator and the rotor. The magneto-motive forces $F_s(d,1\text{-}2)$, $F_s(d{+}1,1\text{-}2)$, $F_r(c,1\text{-}3)$, and $F_r(c{+}1,1\text{-}3)$ are associated with the stator slots d and $d{+}1$, as well as the rotor slots c and $c{+}1$, respectively. The vector $\boldsymbol{\phi}_s$ represents the flux loop vector in the stator, excluding the flux loops present in the stator's air gap denoted as $\boldsymbol{\phi}_{sg}$. Similarly, $\boldsymbol{\phi}_r$ corresponds to the loop flux vector in the rotor, excluding those in the rotor's air gap represented as $\boldsymbol{\phi}_{rg}$. Moreover, $\boldsymbol{V}_{sg}$ and $\boldsymbol{V}_{rg}$ indicate the stator and rotor scalar potential vectors in the air gap region, respectively.

A. Air Gap Coupling

The coupling between the stator and rotor nodes is done using the Lagrange interpolation function [6]. This interpolation function is a high-order polynomial of order n that couples the radial flux density variation in the air gap region and also the scalar potential in the stator V_{s1}-V_{s4} and the rotor V_{r1}-V_{r4}, shown in Figs. 1 (a) and (b) respectively. To obtain a complete coupling between the stator and rotor, additional equations are included in the system matrix. In order to improve the accuracy of the interpolation technique for each MEC block, instead of using a single central angle for each stator and rotor block, k child angles for each block are used. This leads to a total of k^2 combinations between each angle. The average of all combinations is then obtained by dividing the sum of all combinations by k^2. This approach results in a much more accurate interpolation technique, thus improving the overall performance of the MEC model. The stator's scalar potential at a primary stator block j, denoted by V_{sj}, based on the rotor's scalar potential at a primary block w, denoted by V_{rw} is expressed as:

$$V_{sj} = \frac{1}{k^2}\sum_{u=1}^{k}\sum_{v=1}^{k}\sum_{w=1}^{n}\left(V_{rw}\prod_{b=1,b\neq w}^{n}\frac{\theta_{sj_u}-\theta_{rb_v}}{\theta_{rw_v}-\theta_{rb_v}}\right), \quad (1)$$

where the stator angle at a primary block j and a child angle division u is denoted by θ_{sj_u}. In contrast, the rotor angle at a primary block b and a child angle division v is denoted by θ_{rb_v}, and the rotor angle at a primary block w and a child angle division v is denoted by θ_{rw_v}. The third summation and the product indicate the Lagrange interpolation order n for the adjacent main angles. Similarly, the rotor flux density at each block w denoted as B_{rw} can be expressed as a function of the stator flux density at a primary block j, denoted by V_{sj}. The total vector $\boldsymbol{\phi}_{tot}$ to be solved can be expressed as:

$$\boldsymbol{\phi}_{tot} = \begin{bmatrix}\boldsymbol{\phi}_s^{\mathrm{T}} & \boldsymbol{\phi}_{sg}^{\mathrm{T}} & \boldsymbol{V}_{rg}^{\mathrm{T}} & \boldsymbol{\phi}_{rg}^{\mathrm{T}} & \boldsymbol{\phi}_r^{\mathrm{T}} & \boldsymbol{V}_{bo}^{\mathrm{T}}\end{bmatrix}^{\mathrm{T}}, \quad (2)$$

where $\boldsymbol{\phi}_s$ is the flux loop vector in the stator excluding the flux loops in the stator's air gap $\boldsymbol{\phi}_{sg}$, shown in Fig. 1 (a). Similarly, $\boldsymbol{\phi}_r$ is the loop flux vector in the rotor, excluding the ones in the rotor's air gap $\boldsymbol{\phi}_{rg}$, shown in Fig. 1 (b). $\boldsymbol{V}_{rg}$ is the rotor scalar potential vector defined in (1) and $\boldsymbol{V}_{bo}$ is a scalar potential vector to describe the symmetry conditions. In this case the residual function $\boldsymbol{r}$ can be expressed as:

$$\boldsymbol{r} = \mathbf{L}\mathbf{R}_{totd}\mathbf{L}^{\mathrm{T}}\boldsymbol{\phi}_{tot} + \mathbf{G}\boldsymbol{\phi}_{tot} - \left(\mathbf{M}_s\boldsymbol{I}_s(t) + \mathbf{M}_r\boldsymbol{I}_r(t)\right), \quad (3)$$

where $\mathbf{L}$ is a connection matrix of each branch flux and the loop flux [7]. $\mathbf{R}_{totd}$ is a diagonal matrix comprising of all reluctance elements. $\mathbf{G}$ is a matrix that relates the air gap stator loop fluxes $\boldsymbol{\phi}_{sg}$ and rotor loop fluxes $\boldsymbol{\phi}_{rg}$ with the rotor scalar potentials $\boldsymbol{V}_{rg}$ and ensures the equality of the air gap flux densities. In addition, $\mathbf{G}$ includes the relation between the symmetry scalar potential vector $\boldsymbol{V}_{bo}$ and the total flux loop vectors. $\mathbf{M}_s$ and $\mathbf{M}_r$ link each loop flux equation with the corresponding stator phase current vector $\boldsymbol{I}_s$ and rotor loop current vector $\boldsymbol{I}_r$ respectively. $\boldsymbol{I}_s$ and $\boldsymbol{I}_r$ have sizes of $(m\times 1)$ and $(N_r\times 1)$ respectively, where m and N_r are the number of phases and the number of rotor bars respectively.

B. Stator and Rotor Electric Circuit Equations

To include the stator electric circuit, additional equations are required to input the stator voltage at each time step. The model can consider either a star or a delta-connected machine but only a delta-connected one is presented here. For a delta-connected machine, the stator line voltages are applied directly to the terminals of the machine. They are organized into a vector $\boldsymbol{V}_s$ of a size $(m\times 1)$. The phase resistances and end winding inductances are formed in diagonal matrices of $\mathbf{R}_s$ and $\mathbf{L}_s$ respectively. The rotor electric circuit consists of N_r loop current equations that form vector $\boldsymbol{I}_{N_r}$. In each loop, the bar resistance and the end ring resistance are considered to form the rotor resistance matrix $\mathbf{R}_r$. Similarly, the end ring inductance in each loop is used to form the rotor inductance matrix $\mathbf{L}_r$. To consider the broken rotor bars, the conductivity of R_b of a certain bar is controlled to present the fault.

The utilization of the Crank-Nicolson method transforms the stator and rotor time differential equations into finite difference form, which leads to the incorporation of a new residual function $\boldsymbol{r}$.

$$\begin{aligned}\boldsymbol{r} = &\begin{bmatrix}\mathbf{L}\mathbf{R}_{totd}\mathbf{L}^{\mathrm{T}}+\mathbf{G} & -\mathbf{M}_s & -\mathbf{M}_r\\ \frac{q_s}{\Delta t}\mathbf{M}_s^{\mathrm{T}} & \frac{1}{\Delta t}\mathbf{L}_s+\frac{\mathbf{R}_s}{2} & \mathbf{0}\\ \frac{1}{\Delta t}\mathbf{M}_r^{\mathrm{T}} & \mathbf{0} & \frac{1}{\Delta t}\mathbf{L}_r+\frac{\mathbf{R}_r}{2}\end{bmatrix}\begin{bmatrix}\boldsymbol{\phi}_{tot}(k_t)\\ \boldsymbol{I}_s(k_t)\\ \boldsymbol{I}_r(k_t)\end{bmatrix}\\ &-\begin{bmatrix}\mathbf{0} & \mathbf{0} & \mathbf{0}\\ \frac{q_s}{\Delta t}\mathbf{M}_s^{\mathrm{T}} & \frac{1}{\Delta t}\mathbf{L}_s-\frac{\mathbf{R}_s}{2} & \mathbf{0}\\ \frac{1}{\Delta t}\mathbf{M}_r^{\mathrm{T}} & \mathbf{0} & \frac{1}{\Delta t}\mathbf{L}_r-\frac{\mathbf{R}_r}{2}\end{bmatrix}\begin{bmatrix}\boldsymbol{\phi}_{tot}(k_t-1)\\ \boldsymbol{I}_s(k_t-1)\\ \boldsymbol{I}_r(k_t-1)\end{bmatrix}\\ &-\begin{bmatrix}\mathbf{0}\\ \boldsymbol{V}_s(k_t)\\ \mathbf{0}\end{bmatrix},\end{aligned} \quad (4)$$

where q_s represents the number of symmetries considered. Δt is the time step considered between time instants k_t and $k_t - 1$. To minimize mechanical and electrical transients, the suggested approach is to employ a time-harmonic steady-state MEC model. In this model, the time derivatives in the stator electric circuit equations are converted to $-i\omega_s$, where ω_s represents the supply angular frequency. While the time derivatives in the rotor electric circuit equations are converted to $-is\omega_s$, with s denoting the slip of the induction machine. Furthermore, the slip is adjusted until the electromagnetic torque matches the desired input mechanical torque. The output flux loops and currents output from the time-harmonic model are the solution at the first time step for the time-stepping MEC model indicated in (4) for efficient transient reduction.

III. Simulation and Experimental Results

The experimental setup for data collection is illustrated in Fig. 2. In this setup, a 4-pole, 50 Hz induction machine with a power rating of 7.5 kW is employed as the test machine. For every experimental trial, the rotor featuring a broken rotor bar is substituted. Various parameters including speed, torque, and 3-phase currents are measured at a sampling rate of 20 kHz.

All 2D FE and MEC simulations are conducted on a 11th Gen Intel(R) Core(TM) i5-11600 with 32GB installed RAM. Two radial slices are considered to model the skewing effect of the rotor in both the 2D FE and MEC models. The simulations are conducted for 100 cycles, each cycle with 400-time steps. The 2D multi-slice FE models are developed using COMSOL software. The number of triangles in the 2D FE model is 38338 with linear shape function elements for the 2 axial slices. The MEC model has 1380 mesh elements for the stator and 1244 for the rotor for the 2 axial slices.

Various simulation scenarios are performed to test the resilience of the MEC model. These simulations include different conditions, such as a healthy state, one broken rotor bar (1BRB), two broken rotor bars (2BRB), and three broken rotor bars (3BRB). In order to examine the impact of child number divisions k in the Lagrange interpolation, diverse loading conditions are applied to both the experimental setup and the MEC models, specifically for values of k equal to 1 and 3.

The rotor speed of the MEC model, shown in Fig. 3, is compared with the experimental and 2D FE model results for different broken rotor bars at rated loading conditions. The results show that the MEC model can obtain similar speed oscillations and average speed with great accuracy compared to experiments and the 2D FE model. The amplitudes of the harmonic spectrum of the current waveform $\hat{I}_a$ at the steady state of the MEC model, shown in Fig. 4, is compared with the experiments and the 2D FE model for a different number of broken rotor bars at rated loading conditions. It is clear that the MEC and 2D FE models can capture the lower sidebands (LSB) and upper sidebands (USB) amplitudes and frequencies

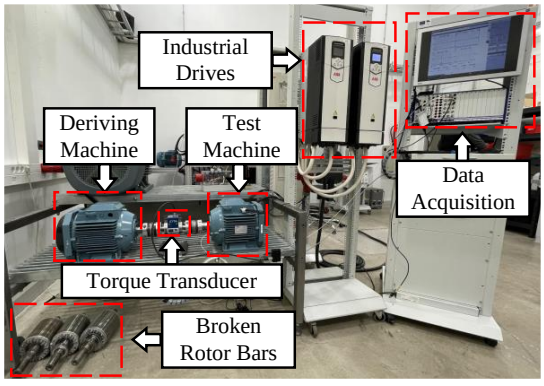

Fig. 2. Measurement setup.

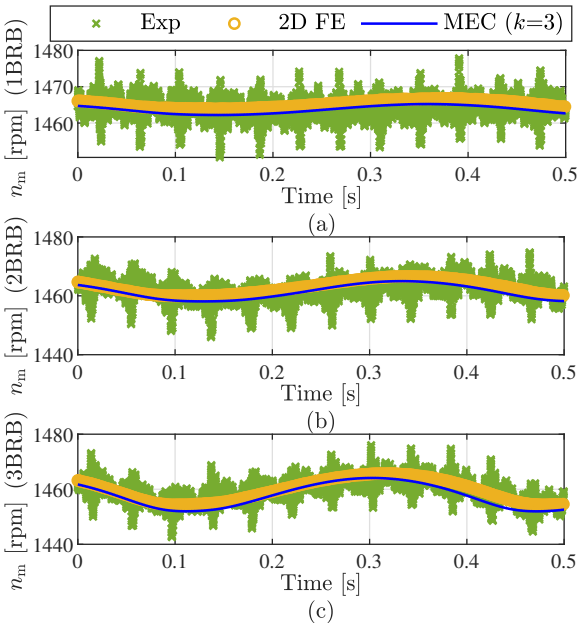

Fig. 3. Rotor speed for different broken bars conditions for the experiments, 2D FE, and MEC models at rated loading condition.

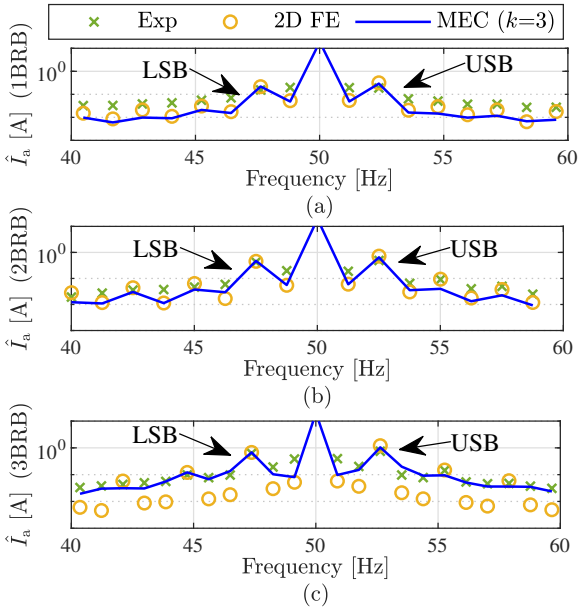

Fig. 4. Harmonic spectrum for the stator phase current for different broken bars conditions for the experiments, 2D FE, and MEC models at rated loading condition.

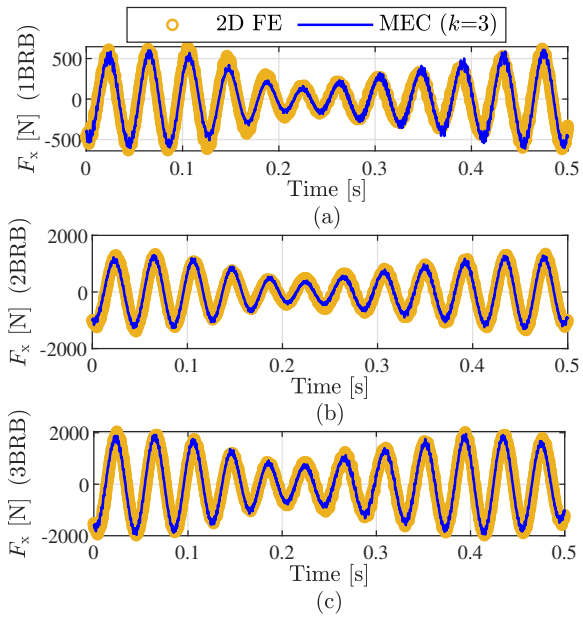

Fig. 5. Forces for different broken bar conditions for FE and MEC models.

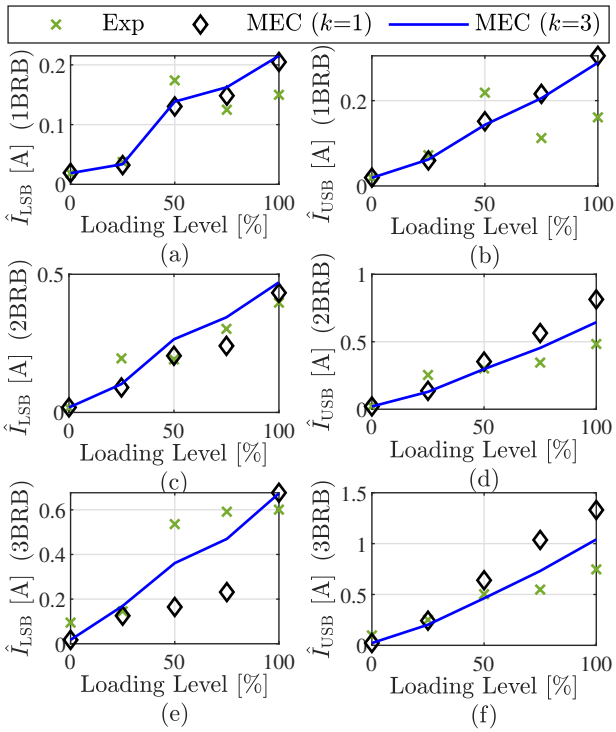

Fig. 6. LSB and USB current amplitudes for different broken bar conditions at different loadings.

of the faults with great accuracy. The horizontal forces F_x are also compared in Fig. 5 for both models for different broken bars at rated loading conditions. The forces are computed using Maxwell's stress tensor [8]. The results show the robustness of the MEC model. To assess the efficacy of the proposed model, varying loading levels are tested in the MEC model, considering different child division numbers, namely k equal to 1 and 3. The investigation also includes one, two, and three broken rotor bars. The amplitudes of the LSB and USB currents denoted as $\hat{I}_{\mathrm{LSB}}$ and $\hat{I}_{\mathrm{USB}}$, are observed. As the number of broken rotor bar increase, the MEC model with k equal to 3 exhibits higher accuracy compared to the case of k equal to 1 for detecting the LSB and USB amplitudes.

Table I shows the CPU time comparison between the 2D FE model and the MEC model for both cases of child number discretizations of k equal to 1 and 3. The table shows that the MEC model is 30 times faster than the 2D FE model without a significant difference between k equal to 1 and 3.

IV. Conclusions

The magnetic equivalent circuit (MEC) model efficiently represents the electromagnetic properties of induction machines, both in healthy and broken bar conditions. Compared to 2D FE models, the MEC model offers high accuracy while requiring shorter computational times. It employs a novel Lagrange interpolation technique, enabling it to effectively capture harmonic sidebands and accurately compute electromagnetic forces during faults. Moreover, the MEC model can serve as valuable input for future vibration analysis purposes and can be extended for various types of electric machines.

TABLE I
CPU time comparison.

	2D FE Model	MEC Model (k = 1)	MEC Model (k = 3)
CPU Time [ms]	1500	54	58

Acknowlegement

This work was supported in part by the Academy of Finland consortium grants 330747 and 46438.

References

[1] A. Singh, B. Grant, R. Defour, C. Sharma, and S. Bahadoorsingh, "A review of induction motor fault modeling," *Electr. Power Syst. Res.*, vol. 133, pp. 191–197, Apr. 2016.

[2] J. Bao, B. L. Gysen, and E. A. Lomonova, "Hybrid analytical modeling of saturated linear and rotary electrical machines: Integration of fourier modeling and magnetic equivalent circuits," *IEEE Trans. Magn.*, vol. 54, Nov. 2018.

[3] G. Y. Sizov, C. C. Yeh, and N. A. Demerdash, "Magnetic equivalent circuit modeling of induction machines under stator and rotor fault conditions," *2009 IEEE Int. Electr. Mach. Drives Conf. IEMDC '09*, pp. 119–124, 2009.

[4] A. M. Silva, C. H. Antunes, A. M. S. Mendes, and F. J. T. E. Ferreira, "Generalized Reluctance Network Framework for Fast Electromagnetic Analysis of Radial-Flux Machines," *IEEE Trans. Energy Convers.*, pp. 1–11, Sep. 2022.

[5] S. Durgam, L. N. Bawankule, and P. S. Khindkar, "Prediction of Fault Detection Based on Vibration Analysis for Motor Applications," *2021 Int. Conf. Nascent Technol. Eng. ICNET 2021 - Proc.*, Jan. 2021.

[6] S. Asfirane, S. Hlioui, S. Mezani, Y. Amara, O. De La Barriere, G. Barakat, and M. Gabsi, "Scalar Magnetic Potential Interpolation for Non-Conformal Meshing in Mesh-Based Generated Reluctance Networks," *IEEE Trans. Magn.*, vol. 55, no. 7, Jul. 2019.

[7] A. Hemeida, A. Lehikoinen, P. Rasilo, H. Vansompel, A. Belahcen, A. Arkkio, and P. Sergeant, "A Simple and Efficient Quasi-3D Magnetic Equivalent Circuit for Surface Axial Flux Permanent Magnet Synchronous Machines," *IEEE Trans. Ind. Electron.*, vol. 66, no. 11, pp. 8318–8333, Nov. 2019.

[8] S. Asfirane, S. Hlioui, Y. Amara, O. D. L. Barriere, G. Barakat, and M. Gabsi, "Global quantities computation using mesh-based generated reluctance networks," *IEEE Trans. Magn.*, vol. 54, Sep. 2018.